Complex-Valued Multifrequency Admittance Model of Three-Phase VSCs in Unbalanced Grids

Yicheng Liao, *Student Member, IEEE*, Xiongfei Wang, *Senior Member, IEEE*, Xiaolong Yue, and Lennart Harnefors, *Fellow, IEEE*

***Abstract*— This article proposes a multifrequency admittance model for voltage-source converters with three-phase unbalanced grid voltages. The model is derived with multiple complex vectors and harmonic transfer functions, which is merely dependent on its own input voltage trajectory, and can accurately capture the frequency-coupling dynamics. The dynamic effects of both the basic synchronous-reference-frame phase-locked loop (PLL) and its alternative with a notch filter of the negative-sequence voltage component are compared. It is revealed that the notch-filtered PLL significantly weakens the frequency-coupling effects, which leads to a reduced order of the admittance model. The developed model is validated by a frequency scan, and the frequency-coupling effects impacted by different PLLs and voltage unbalance factors are verified by the experimental tests. Finally, a case study on stability analysis in unbalanced grids proves the significance of the model.**

***Index Terms*— Complex vector, frequency coupling, harmonic transfer function (HTF), modeling, phase-locked loop (PLL), unbalanced grid, voltage-source converter (VSC).**

I. Introduction

VOLTAGE-SOURCE converters (VSCs) are rapidly increasing in power grids, driven by the widescale use of renewable energy sources and flexible power transmission systems. The small-signal modeling of VSCs becomes important for the stability analysis and controller design of grid-connected VSCs [1].

A fundamental approach to modeling VSCs is to derive time-invariant equilibrium points of the system in the *dq* frame [2], and then the dynamic impacts of different control loops, e.g., the phase-locked loop (PLL), the vector current control, and the dc-link voltage control, can be linearized around the equilibrium points and further analyzed under different grid conditions [3], [4]. However, the *dq*-frame model assumes that the VSC system is three-phase balanced, and consequently the three-phase voltages that are time-periodic operating trajectories can be transformed as the time-invariant operating points in the *dq* frame [5]. As for VSCs with the unbalanced grid voltages, the time-periodic operating trajectories are composed of both positive- and negative-sequence components, which cannot be transformed into time-invariant operating points in a single *dq* frame [6]. Moreover, the unbalanced grid voltage, coupled through the ac–dc power conversion process [7], or asymmetric *dq*-frame control dynamics of the PLL [5] and the dc-link voltage loop [18], leads to more harmonic components in the VSC current, e.g., the nonzero-sequence triplen harmonics [8].

In order to capture the dynamic couplings between different frequency components in three-phase unbalanced systems, the dynamic phasor modeling approach has been developed in [9]–[11]. In the method, with a generalized averaging operator, the time-periodic operating trajectories are modeled by their complex Fourier coefficients, which results in a time-invariant dynamic system [12]. Considering the unbalanced ac voltages, multiple dynamic phasors can be used to model the dynamic couplings of the positive- and negative-sequence subsystems [9], [10]. However, the dynamic phasor model is mostly formulated in the state–space form in the time domain. The explicit frequency-domain representations with frequency coupling transfer function matrices need to be further derived.

Alternatively, the harmonic state–space (HSS) modeling and harmonic transfer functions (HTFs) have been developed [13]–[16]. Unlike the dynamic phasor model, the HSS method linearizes the system directly around the time-periodic trajectories of the system, yielding a linear time-periodic (LTP) system with multifrequency inputs and outputs [13]. Based on the HSS model, the HTF matrices are derived to characterize the dynamic couplings in the frequency domain. Yet, the HTF matrices are derived based on real vectors, which are thus called as real-valued models for brevity. The sequence information of different frequency components in three-phase systems is not revealed in the model, and the HTF matrices are usually of high order [16].

In contrast to the real-vector representations, the multi-frequency model based on the complex vectors is recently reported in [5] and [17]–[19], which is thus called the complex-valued model [20]. With complex vectors, the three-phase balanced voltage or current can be represented by a single variable, which helps reduce the model order. Also, the complex-valued model can intuitively interpret the frequency-coupling dynamics caused by the PLL [5] and the dc-link voltage control [17], [18] in the $\alpha\beta$ frame, since the Park/inverse Park transformations used in the VSC control can be simply seen as frequency shifts by complex vectors in the frequency domain. Alternatively, the complex-valued

Manuscript received September 11, 2019; revised November 20, 2019; accepted December 21, 2019. Date of publication December 31, 2019; date of current version May 6, 2020. Recommended for publication by Associate Editor Xinbo Ruan. *(Corresponding author: Xiongfei Wang.)*

Yicheng Liao and Xiongfei Wang are with the Department of Energy Technology, Aalborg University, 9220 Aalborg, Denmark (e-mail: ycl@et.aau.dk; xwa@et.aau.dk).

Xiaolong Yue is with Ericsson AB, 41756 Gothenburg, Sweden (e-mail: xiaolong_yue@163.com).

Lennart Harnefors is with ABB Corporate Research, 72178 Västerås, Sweden (e-mail: lennart.harnefors@se.abb.com).

Color versions of one or more of the figures in this article are available online at http://ieeexplore.ieee.org.

Digital Object Identifier 10.1109/JESTPE.2019.2963004

model can be built in the dq frame [21], although it only reveals couplings between the dq-frame positive- and negative-sequence subsystems, which still requires a frequency shift when mapping into the phase domain. The mathematical equivalence between the complex-valued $\alpha\beta$-frame and the dq-frame transfer matrices has been established in [5]. However, it is noted that these complex-valued models are all developed for VSCs with three-phase balanced grid voltages.

The use of HTFs for modeling VSCs in unbalanced grids has been recently reported in [22]. The model is derived based on the symmetrical component decomposition, which is essentially equivalent to the complex-vector representations in the $\alpha\beta$ frame [18]. However, the model is introduced as the sequence impedance, which leads to ambiguous interpretation when the negative-frequency components in the negative sequence are generated by the frequency couplings. Moreover, only the basic synchronous-reference-frame (SRF)-PLL is considered in [22], which is impractical for VSCs operating in unbalanced grids, since it has poor attenuation on the negative-sequence voltage. In addition, using the SRF-PLL causes more complex frequency couplings, which results in a high-order HTF matrix and poses challenges to the model truncation [23]. However, only the frequency couplings caused by the asymmetrical grid structure is considered in [22], while the coupling effect of the unbalanced operating trajectory on the PLL is overlooked.

Considering the coupling effect of an unbalanced operating trajectory on the PLL, this article proposes a generalized multifrequency admittance model for VSCs under unbalanced grid conditions. First, the concepts of base vectors in the complex space are introduced to rigorously characterize the frequency-coupling dynamics of VSCs. Then, the dynamic impact of the SRF-PLL with a notch filter used for removing the negative-sequence voltage component is analyzed and further compared with that of the basic SRF-PLL. It is explicitly revealed that the notch-filtered PLL can significantly weaken the couplings of different frequency components, leading to a reduced-order model. Furthermore, different from [22], the multifrequency admittance model is merely dependent on the unbalanced operating trajectory of the VSC, rather than the grid impedance, and thus it can be readily applied to assess the dynamic interactions of VSCs with different unbalanced grid impedances. Finally, the proposed model is validated by the frequency scan, and the frequency-coupling effects of the VSC in unbalanced grids are verified in experiments. The significance of the proposed model for stability analysis in unbalanced grids is also proved by a case study.

II. Steady-State Analysis

The three-phase three-wire VSC system with three-phase unbalanced grid voltage is studied. Fig. 1 shows the single-line represented diagram of the system, where υ denotes the unbalanced grid voltage input and $Z_{\rm ac}$ represents the ac-side three-phase filter, which can be L or LCL filter. A PLL is used for grid synchronization, and a proportional and resonant (PR) current controller (CC) in the $\alpha\beta$ frame is implemented. Since no other outer loop is considered, the current references, $I_{d\rm ref}$ and $I_{q\rm ref}$, are given as constant.

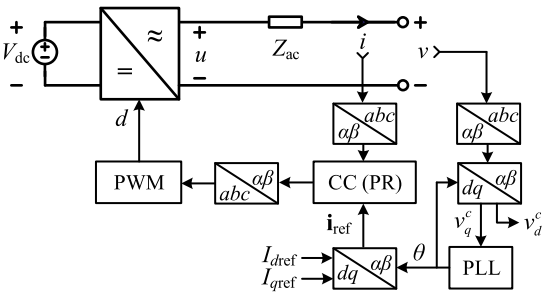

Fig. 1. Single-line representation for a VSC system.

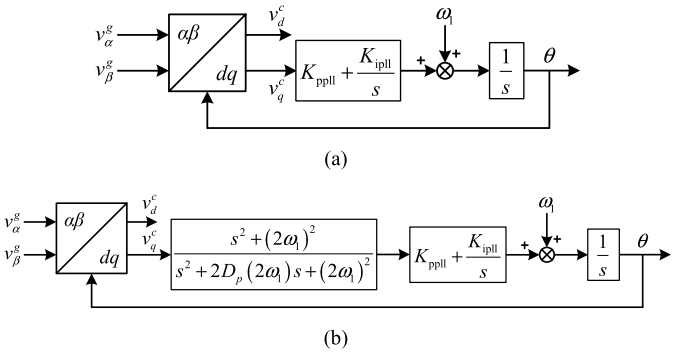

Fig. 2. Control diagrams of PLLs. (a) SRF-PLL. (b) Notch-SRF-PLL.

It has been reported that the PLL brings frequency-coupling dynamics in VSCs [1], [5]. To study its dynamic impact with unbalanced voltages, the steady-state analysis is performed first. Fig. 2 shows the control diagrams of a basic SRF-PLL and an SRF-PLL with a notch filter (Notch-SRF-PLL) that is used to remove the negative-sequence voltage component.

A. Linearization of Park Transformation

The Park transformation used in the PLL transforms the grid voltage from the $\alpha\beta$ frame to the control dq frame, which can be represented as

$$\begin{bmatrix} v_d^c \\ v_q^c \end{bmatrix} = \begin{bmatrix} \cos\theta & \sin\theta \\ -\sin\theta & \cos\theta \end{bmatrix} \begin{bmatrix} v_\alpha^g \\ v_\beta^g \end{bmatrix} \triangleq \mathbf{P}_\theta \begin{bmatrix} v_\alpha^g \\ v_\beta^g \end{bmatrix}. \tag{1}$$

If $\Delta\theta$ is defined as the difference between the locked phase θ and the positive-sequence voltage phase θ^+, there exists

$$\begin{bmatrix} v_d^c \\ v_q^c \end{bmatrix} = \mathbf{P}_\theta \begin{bmatrix} v_\alpha^g \\ v_\beta^g \end{bmatrix} = \mathbf{P}_{\Delta\theta}\mathbf{P}_{\theta^+} \begin{bmatrix} v_\alpha^g \\ v_\beta^g \end{bmatrix} \triangleq \mathbf{P}_{\Delta\theta} \begin{bmatrix} v_d^g \\ v_q^g \end{bmatrix} \tag{2}$$

where $\Delta\theta$ also denotes the angle between the control dq frame and the grid dq frame in steady state, which is illustrated in Fig. 3. Thus, it can be derived that

$$v_d^c = v_d^g \cos\Delta\theta + v_q^g \sin\Delta\theta \tag{3a}$$

$$v_q^c = v_q^g \cos\Delta\theta - v_d^g \sin\Delta\theta. \tag{3b}$$

It is worth noting that all the variables in (3) are time-periodic in steady state with the unbalanced voltage input [23]; thus, their derivatives are nonzero and the system

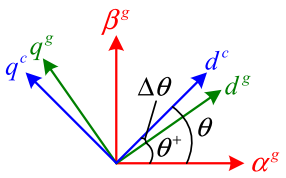

Fig. 3. Relationship among the grid $\alpha\beta$ frame, the grid dq frame, and the control dq frame.

TABLE I
GRID VOLTAGE AND PLL PARAMETERS

Parameters	Symbols	Values
Grid voltage	V^+ V^-	1.0 p.u. (100 V) 0.6 p.u. / 0.1 p.u.
Fundamental angular frequency	ω_1	2π·50 rad/s
PLL PI controller	K_{ppll} K_{ipll} BW	5 rad/(s·V) / 1 rad/(s·V) 100 rad/(s²·V) / 27 rad/(s²·V) 82 Hz / 20 Hz
Notch filter damping factor	D_{p}	0.707

has no equilibrium point [24]. Linearizing (3b) around its steady-state trajectory yields

$$\begin{aligned} V_q^c + \hat{v}_q^c &= \left(V_q^g + \hat{v}_q^g\right)\cos\left(\Delta\theta + \hat{\theta}\right) \\ &\quad - \left(V_d^g + \hat{v}_d^g\right)\sin(\Delta\theta + \hat{\theta}) \\ \Rightarrow V_q^c + \hat{v}_q^c &\approx \underbrace{\left(V_q^g\cos\Delta\theta - V_d^g\sin\Delta\theta\right)}_{V_q^c} + \cos\Delta\theta\cdot\hat{v}_q^g \\ &\quad - \sin\Delta\theta\cdot\hat{v}_d^g - \underbrace{\left(V_q^g\sin\Delta\theta + V_d^g\cos\Delta\theta\right)}_{V_d^c}\cdot\hat{\theta} \end{aligned} \tag{4}$$

where the small letters with "^" represent small-signal perturbations, and the capital letters denote steady states. It is clear that $\hat{v}_q^c$ is determined by $\hat{v}_d^g$, $\hat{v}_q^g$, and $\hat{\theta}$ through three time-periodically varying coefficients, i.e., $\sin\Delta\theta(t)$, $\cos\Delta\theta(t)$, and $V_d^c(t)$. Hence, to model the dynamic coupling of the PLL with unbalanced voltages, it is important to perform a steady-state analysis of the time-periodic operating trajectories first.

B. Steady-State Analysis

In the steady-state analysis, three cases with different PLL parameters and unbalanced grid voltages are considered. Table I provides the parameters of grid voltages and PLLs. V^+ and V^- denote the magnitudes of the positive- and negative-sequence voltage components at the fundamental frequency. The voltage unbalanced factor (VUF), which is defined as VUF $= V^-/V^+$, is changed by V^-. The PLL control bandwidth (BW) is changed with different proportional and integral (PI) control parameters, and the three cases analyzed are listed as follows.

1) Case A: $V^- = 0.6$ p.u. (VUF $= 0.6$) and PLL BW $=$ 82 Hz.
2) Case B: $V^- = 0.1$ p.u. (VUF $= 0.1$) and PLL BW $=$ 82 Hz.
3) Case C: $V^- = 0.6$ p.u. (VUF $= 0.6$) and PLL BW $=$ 20 Hz.

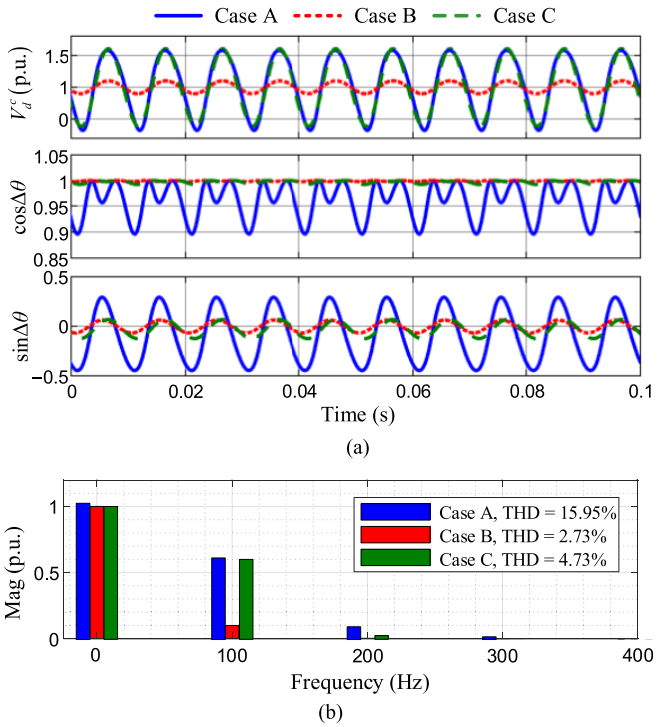

Fig. 4. Steady-state analysis of the SRF-PLL for Cases A–C. (a) Time-domain waveforms. (b) Spectrum of $V_d^c(t)$.

1) SRF-PLL: Fig. 4 shows the steady-state analysis of $\sin\Delta\theta(t)$, $\cos\Delta\theta(t)$, and $V_d^c(t)$ for the SRF-PLL in Cases A–C. It can be seen from Fig. 4(a) that the approximations that $\sin\Delta\theta \approx 0$ and $\cos\Delta\theta \approx 1$ are invalid due to the nonnegligible $\Delta\theta$, e.g., in Case A. The three variables are all time-periodic.

Furthermore, from the spectrum of $V_d^c(t)$ in Fig. 4(b), it can be observed that the steady-state harmonics are not fixed, which are closely related to the VUF and the PLL BW. Theoretically, the nonnegligible $\Delta\theta$ and the unbalanced input voltage can lead to infinite harmonics in the three time-periodic operating trajectories, ranging from 0 rad/s to $\pm 2k\omega_1 (k\epsilon\mathbb{Z}^+$, where $\mathbb{Z}^+$ is the positive integer set and ω_1 is the fundamental angular frequency). For further illustration, the total harmonic distortion (THD) of $V_d^c(t)$ by removing its dc component is analyzed under different cases. The fundamental frequency becomes 100 Hz in $V_d^c(t)$ because of the Park transformation applied to the negative-sequence component. The analyzed THDs are given in the legend in Fig. 4(b). It is found that the THD of $V_d^c(t)$ can change with the VUF and the PLL BW in the SRF-PLL.

2) Notch-SRF-PLL: For the Notch-SRF-PLL, the steady-state analysis of Cases A–C is provided in Fig. 5. It is clear that with the Notch-SRF-PLL, the assumptions of $\sin\Delta\theta \approx 0$ and $\cos\Delta\theta \approx 1$ can be justified. The locked phase θ aligns well with θ^+, i.e., $\Delta\theta \approx 0$ in steady state. $V_d^c(t)$ contains only fixed harmonic orders, i.e., 0 rad/s and $\pm 2\omega_1$ with zero THD due to the attenuation of the negative-sequence voltage by the notch filter. The VUF affects only the magnitude of the harmonic component at $\pm 2\omega_1$ in $V_d^c(t)$.

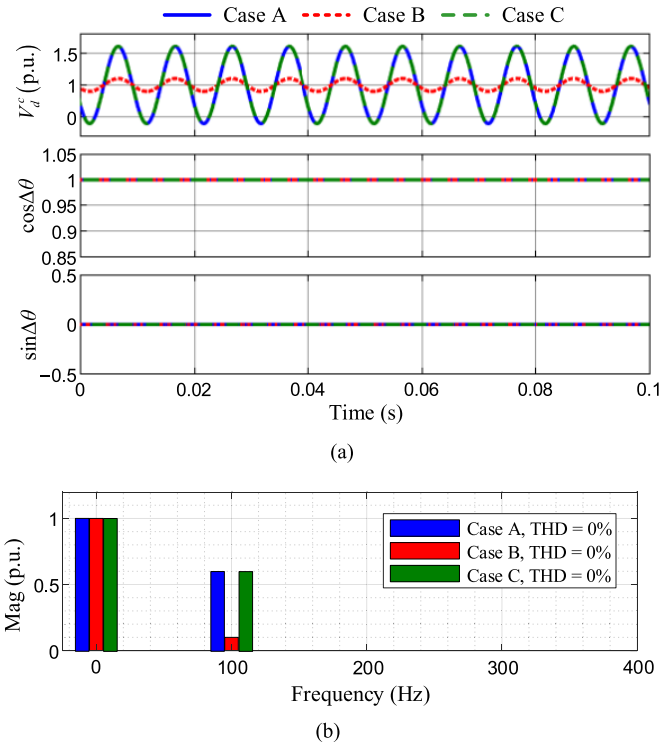

Fig. 5. Steady-state analysis of the Notch-SRF-PLL for Cases A–C. (a) Time-domain waveforms. (b) Spectrum of $V_d^c(t)$.

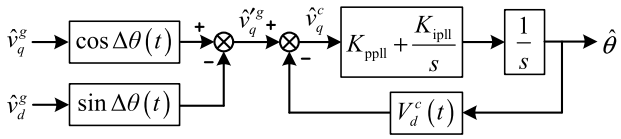

Fig. 6. Small-signal model of SRF-PLL with unbalanced voltages.

The steady-state analyses indicate that the unbalanced grid voltage leads to the time-periodic trajectories for both PLLs, which introduce the LTP dynamic behavior to the system [13]. To further characterize the LTP dynamics in the frequency domain, both PLLs are modeled with HTFs based on the HSS theory in Section III.

III. PLL Modeling

This section derives the HTF models of both PLLs in the real *dq* frame first, and then transforms them into the complex *dq* frame and the complex $\alpha\beta$ frame by using complex vectors.

A. SRF-PLL in Real DQ Frame

Based on the linearization of (4), the small-signal model of the SRF-PLL can be obtained as shown in Fig. 6. The HTFs of the three time-periodic coefficients can be represented by Toeplitz matrices with their Fourier coefficients as constant elements [13]–[16]. The PI and I controllers used in the SRF-PLL are linear time-invariant (LTI), whose HTF can be represented by a diagonal matrix, where each element is a transfer function of $s \pm j2k\omega_1$.

With HTFs, Fig. 7 illustrates the dynamic propagations of different frequency components in the SRF-PLL, where each block represents an HTF. $\mathcal{V}_d^c$, $\mathcal{T}_{\cos\Delta\theta}$, and $\mathcal{T}_{\sin\Delta\theta}$ are the HTFs of the time-periodic coefficients, and $\mathcal{G}_{\text{PI}-\text{I}}(s)$ is the HTF of the PI and I controllers, which have been derived in [23].

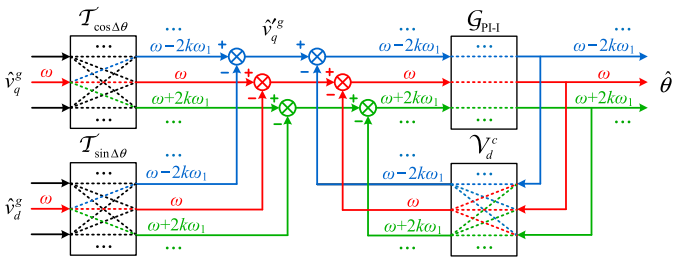

Fig. 7. Frequency-domain dynamic propagations of SRF-PLL.

If a perturbation at a frequency of ω is imposed at the input voltage $\hat{v}_d^g$ or $\hat{v}_q^g$, there will be responses at the frequencies of ω and $\omega \pm 2k\omega_1$ generated in the locked phase. The variables in Fig. 7 are thus n-dimensional (n-D) (where $n = 2k+1$) in the frequency domain, which can be represented by

$$\hat{\theta} \leftrightarrow \boldsymbol{\Theta}(s) = \left[\ldots \quad \hat{\theta}(s - j2\omega_1) \quad \hat{\theta}(s) \quad \hat{\theta}(s + j2\omega_1) \quad \ldots\right]^{\text{T}} \tag{5}$$

$$\hat{v}_d^g \leftrightarrow \mathbf{V}_d^g(s) = \left[\ldots \quad \hat{v}_d^g(s - j2\omega_1) \quad \hat{v}_d^g(s) \quad \hat{v}_d^g(s + j2\omega_1) \quad \ldots\right]^{\text{T}} \tag{6}$$

where the frequency shifts, i.e., $s \pm j2k\omega_1$, capture the frequency couplings caused by the nonnegligible $\Delta\theta$ and the unbalanced input voltage. Similar expressions apply to other variables also, e.g., $\hat{v}_q^g \leftrightarrow \mathbf{V}_q^g(s)$ and $\hat{v}_q'^g \leftrightarrow \mathbf{V}'^g_q(s)$. Consequently, the HTF model of the SRF-PLL can be derived as

$$\boldsymbol{\Theta}(s) = \underbrace{\left(\mathcal{I} + \mathcal{G}_{\text{PI-I}}(s)\mathcal{V}_d^c\right)^{-1}\mathcal{G}_{\text{PI-I}}(s)}_{[\mathcal{G}_{\text{PLL}}(s)]_{n\times n}} \times \underbrace{\left(\mathcal{T}_{\cos\Delta\theta}\mathbf{V}_q^g(s) - \mathcal{T}_{\sin\Delta\theta}\mathbf{V}_d^g(s)\right)}_{\mathbf{V}'^g_q(s)} \tag{7}$$

where $\mathcal{I}$ is an identity matrix. Theoretically, the derived HTF model, i.e., $\mathcal{G}_{\text{PLL}}(s)$, is an infinite $n \times n$ matrix with $n = 2k+1$, which is denoted by "$[]_{n\times n}$." However, in practice, the model has to be truncated into a finite order, by identifying dominant harmonics in the time-periodic coefficients. According to Fig. 4, the value of k can be determined based on the dominant harmonics in $V_d^c(t)$, which varies from the VUF and the PLL BW.

B. Notch-SRF-PLL in Real DQ Frame

For the notch-SRF-PLL, $\Delta\theta$ becomes zero in steady state, and hence, the small-signal model of the notch-SRF-PLL can be drawn as shown in Fig. 8. Unlike the SRF-PLL, there is only one time-periodic coefficient, i.e., $V_d^c(t)$. Moreover, $V_d^c(t)$ only contains steady-state harmonics of 0 rad/s and $\pm 2\omega_1$ according to Fig. 5, regardless of the change of VUF and PLL BW. These features also apply to other alternative filtered SRF-PLLs.

The HTF model of the Notch-SRF-PLL is derived as

$$\boldsymbol{\Theta}(s) = \underbrace{\left(\mathcal{I} + \mathcal{G}_{\text{Notch-PI-I}}(s)\mathcal{V}_d^c\right)^{-1}\mathcal{G}_{\text{Notch-PI-I}}(s)}_{[\mathcal{G}_{\text{PLL}}(s)]_{3\times 3}}\mathbf{V}_q^g(s) \tag{8}$$

where $\mathcal{G}_{\text{Notch}-\text{PI}-\text{I}}(s)$ is the HTF of the notch filter, the PI, and I controllers. The derived $\mathcal{G}_{\text{PLL}}(s)$ has the fixed order with

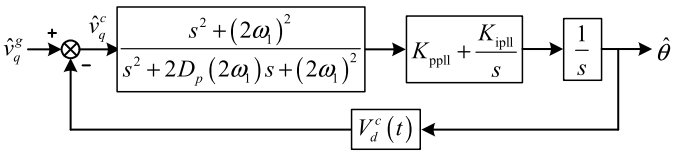

Fig. 8. Small-signal model of notch-SRF-PLL with unbalanced voltages.

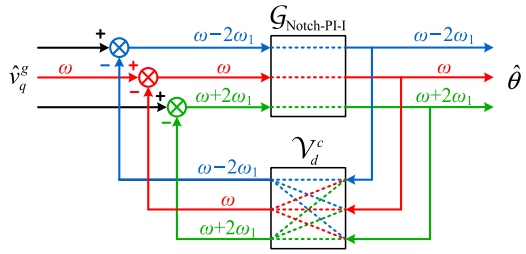

Fig. 9. Frequency-domain dynamic propagations of notch-SRF-PLL.

TABLE II
COMPARISON OF SRF-PLL AND NOTCH-SRF-PLL

Input voltage	Features	SRF-PLL	Notch-SRF-PLL
Balanced	Steady-state variables (harmonic spectrum)	V_d^c (0 rad/s)	V_d^c (0 rad/s)
	Dynamic property	LTI	LTI
Unbalanced	Steady-state variables (harmonic spectrum)	$\cos\Delta\theta$ (0 rad/s, $\pm 2k\omega_1$) $\sin\Delta\theta$ (0 rad/s, $\pm 2k\omega_1$) V_d^c (0 rad/s, $\pm 2k\omega_1$)	V_d^c (0 rad/s, $\pm 2\omega_1$)
	Impact factors of steady-state harmonic spectrum	VUF and PLL BW (impacting dominant harmonic order and magnitude)	VUF (impacting magnitude only)
	Dynamic property	LTP ($n\times n$ HTF, $n=2k+1$)	LTP (3×3 HTF)

$n = 3$ ($k = 1$); thus, the dynamic propagations of different frequency components are depicted in Fig. 9. It is seen that the use of a notch filter significantly weakens the frequency couplings compared with that in Fig. 7.

C. Comparison of SRF-PLL and Notch-SRF-PLL

According to the steady-state analyses, the SRF-PLL and the Notch-SRF-PLL are compared in Table II. Both PLLs behave as LTI systems with the balanced voltage input, yet become LTP systems with the unbalanced voltage input.

For the SRF-PLL, the steady-state variables that influence the linearization include $\cos\Delta\theta(t)$, $\sin\Delta\theta(t)$, and $V_d^c(t)$. Their harmonic spectrum contains infinite components at 0 rad/s and $\pm 2k\omega_1$, whose magnitude and dominant harmonic order are impacted by the VUF and the PLL BW. Therefore, an $n \times n$ HTF model is needed to characterize the frequency coupling dynamics.

For the Notch-SRF-PLL, $V_d^c(t)$ is the only steady-state variable that influences the linearization. It contains merely three harmonic components, i.e., 0 rad/s and $\pm 2\omega_1$, which leads to a 3×3 HTF model. The VUF only impacts the magnitude of the component at $\pm 2\omega_1$ in $V_d^c(t)$. These features also apply to other prefiltered SRF-PLLs, since they are all capable of filtering out the negative-sequence component in the input voltage.

D. PLL Model Representation in Complex Space

The HTFs given by (7) and (8) are both derived in the real dq frame, where only the frequency-coupling dynamics caused by the time-periodic trajectories are characterized. In addition, frequency couplings can also be introduced in VSCs by asymmetric dq-frame control loops [5], [18]. Therefore, (7) and (8) are further transformed into the complex space and the $\alpha\beta$ frame.

The concept of base vectors in the complex space is introduced to represent system variables, which are defined as follows [18], [25]:

$$\begin{bmatrix} v_\alpha \\ v_\beta \end{bmatrix} \Leftrightarrow \begin{bmatrix} \mathbf{v} \\ \mathbf{v}^* \end{bmatrix} = \begin{bmatrix} v_\alpha + jv_\beta \\ v_\alpha - jv_\beta \end{bmatrix} \tag{9}$$

$$\begin{bmatrix} v_d \\ v_q \end{bmatrix} \Leftrightarrow \begin{bmatrix} \mathbf{v}_{dq} \\ \mathbf{v}_{dq}^* \end{bmatrix} = \begin{bmatrix} v_d + jv_q \\ v_d - jv_q \end{bmatrix} \tag{10}$$

where the real vectors in the $\alpha\beta$- and dq-frames represented by $[v_\alpha, v_\beta]^{\mathrm{T}}$ and $[v_d, v_q]^{\mathrm{T}}$ are mapped as two base vectors in the complex space, i.e., $[\mathbf{v}, \mathbf{v}^*]^{\mathrm{T}}$ and $[\mathbf{v}_{dq}, \mathbf{v}_{dq}^*]^{\mathrm{T}}$, and "$*$" denotes the complex conjugate operator. Therefore, the model derived based on complex vectors in the complex space is called a complex-valued model [8], [18]–[20].

It is worth noting that the two base vectors in the $\alpha\beta$ frame are equivalent to the time-dependent sequence components of three-phase three-wire systems introduced in [26], except a scaling factor, which can be 1/2 or $\sqrt{2}/2$ for the magnitude-invariant or the power-invariant form. However, the two base vectors in the dq frame have no direct implications on sequence components of three-phase systems.

Based on (9) and (10), the relationship from the input voltage to the locked phase for the SRF-PLL can be derived as

$$\begin{aligned} \hat{\theta} &= \mathcal{G}_{\text{PLL}}(p)\hat{v}_q^c = \mathcal{G}_{\text{PLL}}(p)\text{Im}\{e^{-j\Delta\theta}\hat{\mathbf{v}}_{dq}^g\} \\ &\overset{dq\text{frame}}{=} \frac{1}{2j}[\mathcal{G}_{\text{PLL}}(p)e^{-j\Delta\theta} \quad -\mathcal{G}_{\text{PLL}}(p)e^{j\Delta\theta}] \begin{bmatrix} \hat{\mathbf{v}}_{dq}^g \\ \hat{\mathbf{v}}_{dq}^{g*} \end{bmatrix} \\ &\overset{\alpha\beta\text{frame}}{=} \frac{1}{2j}\left[\mathcal{G}_{\text{PLL}}(p)\, e^{-j\theta^+}e^{-j\Delta\theta} \quad -\mathcal{G}_{\text{PLL}}(p)\, e^{-j\theta^+}e^{j\Delta\theta}\right] \\ &\quad \times \begin{bmatrix} \hat{\mathbf{v}}^g \\ e^{j2\theta^+}\hat{\mathbf{v}}^{g*} \end{bmatrix} \end{aligned} \tag{11}$$

where p denotes the derivative operator with $p = d/dt$, corresponding to the Laplace transform variable s in the frequency domain. $e^{-j\Delta\theta}$ and $e^{j\Delta\theta}$ denote the Park transformation and the inverse Park transformation of $\Delta\theta$ in complex space, respectively, and their complex transfer matrices can be given by the HTFs of $\cos\Delta\theta(t)$ and $\sin\Delta\theta(t)$, that is,

$$e^{-j\Delta\theta} \leftrightarrow \mathcal{T}_{\cos\Delta\theta} - j\mathcal{T}_{\sin\Delta\theta} \triangleq \mathcal{T}_{\Delta\theta}^* \tag{12}$$

$$e^{j\Delta\theta} \leftrightarrow \mathcal{T}_{\cos\Delta\theta} + j\mathcal{T}_{\sin\Delta\theta} \triangleq \mathcal{T}_{\Delta\theta}. \tag{13}$$

It is noted that (11) using complex vectors is a time-domain representation, which thus only has two inputs. Each complex vector is represented by an n-D vector in the frequency domain, according to (5) and (6). Thus, all the time-domain

operators, i.e., $\mathcal{G}_{\rm PLL}(p)$, $e^{-j\Delta\theta}$ and $e^{j\Delta\theta}$, can then be represented by $n \times n$ HTFs in the frequency domain. It is also seen that the voltage dynamics from the two base vectors have different impacts on the locked phase.

The model for the Notch-SRF-PLL can be derived in a similar way, although the impacts of $e^{-j\Delta\theta}$ and $e^{j\Delta\theta}$ can be ignored, i.e., $\mathcal{T}_{\Delta\theta}$ can be regarded as an identity matrix.

IV. VSC Modeling

The VSC model considering the dynamics of both the PLL and CC is derived in this section.

A. PLL Impacts on Current Reference Generation

As can be seen from Fig. 1, the dynamic of PLL affects the current reference through an inverse Park transformation, that is,

$$\mathbf{i}_{\rm ref} = e^{j\theta}\mathbf{i}_{dq\rm ref} \tag{14}$$

whose small-signal model is derived as

$$\begin{aligned}\hat{\mathbf{i}}_{\rm ref} &= e^{j\Delta\theta}e^{j\theta^+}\hat{\mathbf{i}}_{dq\rm ref} + jI_{dq\rm ref}e^{j\Delta\theta}e^{j\theta^+}\hat{\theta}\\ &\overset{\hat{\mathbf{i}}_{dq\rm ref}=0}{=} jI_{dq\rm ref}e^{j\Delta\theta}e^{j\theta^+}\hat{\theta}\\ &= \frac{I_{dq\rm ref}}{2}[e^{j\Delta\theta}\mathcal{G}_{\rm PLL}(p-j\omega_1)e^{-j\Delta\theta}\\ &\qquad - e^{j\Delta\theta}\mathcal{G}_{\rm PLL}(p-j\omega_1)e^{j\Delta\theta}]\begin{bmatrix}\hat{\mathbf{v}}^g\\ e^{j2\theta^+}\hat{\mathbf{v}}^{g*}\end{bmatrix}\end{aligned} \tag{15}$$

where $I_{dq\rm ref}$ is the steady-state current reference, which is a constant given by $I_{d\rm ref} + jI_{q\rm ref}$. $\hat{\mathbf{i}}_{dq\rm ref}$ is assumed to be zero in this derivation as no outer loop control is considered. The small-signal diagrams of the PLL and the current reference generation are shown in the dashed boxes in Fig. 10(a).

To unify the forms of input and output variables, the conjugate operation and an angle rotation of $e^{j2\theta^+}$ are applied to (15) successively, yielding the small-signal denotations by the dashed arrows in Fig. 10(a). Combining the dual inputs and dual outputs, and reformulating the small-signal diagram of Fig. 10(a) yields

$$\begin{bmatrix}\hat{\mathbf{i}}_{\rm ref}\\ e^{j2\theta^+}\hat{\mathbf{i}}^*_{\rm ref}\end{bmatrix} = \mathbf{Y}_{\rm PLL}(p)\begin{bmatrix}\hat{\mathbf{v}}^g\\ e^{j2\theta^+}\hat{\mathbf{v}}^{g*}\end{bmatrix} \tag{16}$$

where $\mathbf{Y}_{\rm PLL}(p)$ is given by (17) shown at the bottom of this page. In (16), the input vector consists of two complex vectors. For the second complex vector, there is an additional operator of $e^{j2\theta^+}$, which is the leftover of the PLL control transformed into the complex $\alpha\beta$ frame. $\mathbf{Y}_{\rm PLL}(s)$ is defined as the complex transfer matrix from the grid voltage to the current reference, which can be derived from (12) and (13) as

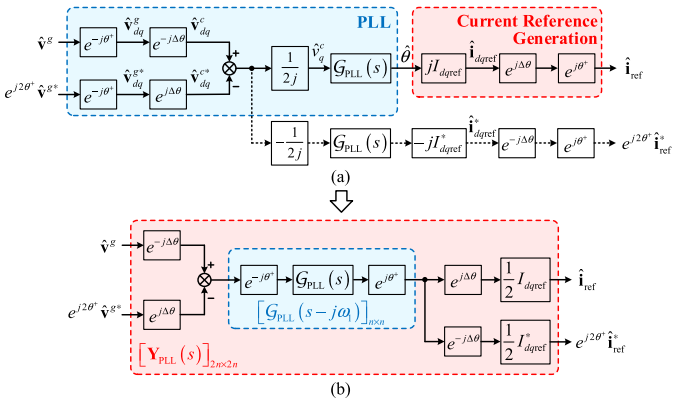

Fig. 10. Derivation of $\mathbf{Y}_{\rm PLL}(s)$. (a) Small-signal diagrams of the PLL and the current reference generation. (b) Small-signal diagram from the grid voltage to the current reference in the complex space.

(18) shown at the bottom of this page, whose block diagram is shown in Fig. 10(b). According to (6), each voltage complex vector is denoted by an n-D vector in the frequency domain; thus, the time-domain 2-D input in (16) corresponds to a $2n$-D vector in the frequency domain, that is,

$$\begin{aligned}\begin{bmatrix}\hat{\mathbf{v}}^g\\ e^{j2\theta^+}\hat{\mathbf{v}}^{g*}\end{bmatrix} &\leftrightarrow \begin{bmatrix}\cdots\\ \mathbf{V}^g(s-j2\omega_1)\\ \mathbf{V}^g(s)\\ \mathbf{V}^g(s+j2\omega_1)\\ \cdots\\ \cdots\\ e^{j2\varphi^+}\mathbf{V}^{g*}((s-j2\omega_1)-j2\omega_1)\\ e^{j2\varphi^+}\mathbf{V}^{g*}(s-j2\omega_1)\\ e^{j2\varphi^+}\mathbf{V}^{g*}((s+j2\omega_1)-j2\omega_1)\\ \cdots\end{bmatrix}\\ &= \begin{bmatrix}\cdots\\ \mathbf{V}^g(s-j2\omega_1)\\ \mathbf{V}^g(s)\\ \mathbf{V}^g(s+j2\omega_1)\\ \cdots\\ \cdots\\ e^{j2\varphi^+}\mathbf{V}^{g*}(s-j4\omega_1)\\ e^{j2\varphi^+}\mathbf{V}^{g*}(s-j2\omega_1)\\ e^{j2\varphi^+}\mathbf{V}^{g*}(s)\\ \cdots\end{bmatrix}.\end{aligned} \tag{19}$$

In (19), the first – nth elements denote the frequency responses of $\hat{\mathbf{v}}^g$, which are derived simply by the frequency shifts of $\pm 2k\omega_1$ based on s. This is caused by the time-periodic operating trajectory. It is worth noting that the vector $\hat{\mathbf{v}}^g$ does not always imply the positive-sequence component, since the negative-sequence component will be generated

$$\mathbf{Y}_{\rm PLL}(p) = \frac{1}{2}\begin{bmatrix} I_{dq\rm ref}e^{j\Delta\theta}\mathcal{G}_{\rm PLL}(p-j\omega_1)e^{-j\Delta\theta} & -I_{dq\rm ref}e^{j\Delta\theta}\mathcal{G}_{\rm PLL}(p-j\omega_1)e^{j\Delta\theta}\\ -I^*_{dq\rm ref}e^{-j\Delta\theta}\mathcal{G}_{\rm PLL}(p-j\omega_1)e^{-j\Delta\theta} & I^*_{dq\rm ref}e^{-j\Delta\theta}\mathcal{G}_{\rm PLL}(p-j\omega_1)e^{j\Delta\theta}\end{bmatrix} \tag{17}$$

$$\mathbf{Y}_{\rm PLL}(s) = \frac{1}{2}\begin{bmatrix} I_{dq\rm ref}\mathcal{T}_{\Delta\theta}\mathcal{G}_{\rm PLL}(s-j\omega_1)\mathcal{T}^*_{\Delta\theta} & -I_{dq\rm ref}\mathcal{T}_{\Delta\theta}\mathcal{G}_{\rm PLL}(s-j\omega_1)\mathcal{T}_{\Delta\theta}\\ -I^*_{dq\rm ref}\mathcal{T}^*_{\Delta\theta}\mathcal{G}_{\rm PLL}(s-j\omega_1)\mathcal{T}^*_{\Delta\theta} & I^*_{dq\rm ref}\mathcal{T}^*_{\Delta\theta}\mathcal{G}_{\rm PLL}(s-j\omega_1)\mathcal{T}_{\Delta\theta}\end{bmatrix} \tag{18}$$

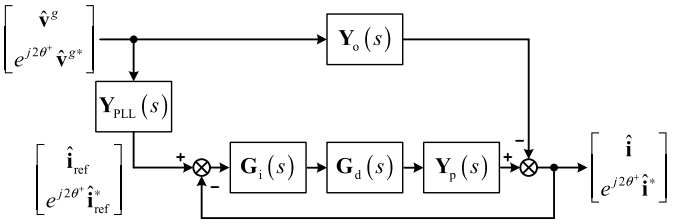

Fig. 11. Small-signal model of the VSC in the complex-valued multifrequency frame.

when the resulted frequency is negative. The $(n+1)$th–$2n$th elements represent the frequency responses of $e^{j2\theta^+}\hat{\mathbf{v}}^{g*}$, and the corresponding frequencies are derived by the frequency shifts of $-2\omega_1$ applied to all the frequency components of $\hat{\mathbf{v}}^g$. This frequency shift is resulted from the operator $e^{j2\theta^+}$. Similarly, the frequency responses in $e^{j2\theta^+}\hat{\mathbf{v}}^{g*}$ are not always negative-sequence components, and they may become positive-sequence components if the corresponding frequencies are negative. In addition to the frequency shift, the initial phase of the positive-sequence voltage, i.e., $e^{j2\varphi^+}$, has to be considered in the frequency responses, which indicates the phase-dependent property of the system [18].

The transfer matrix in (18) can be regarded as a matrix with four block matrices, and each block matrix is an $n \times n$ HTF model. Hence, the additional frequency-coupling dynamics caused by the PLL are characterized by the coupled HTFs between the two base vectors in the $\alpha\beta$ frame. Consequently, the PLL dynamics is represented by a $2n \times 2n$ complex transfer matrix, i.e., $\mathbf{Y}_{\mathrm{PLL}}(s)$.

B. VSC Model

In addition to the PLL, the CC, the time delay, and the converter power stage are modeled. They can be treated as linear systems [5], whose HTF models in the complex $\alpha\beta$ frame are derived as follows.

Given an LTI transfer function $G(s)$ in the $\alpha\beta$ frame, it can be represented in a unified form adaptive to (19), leading to a $2n \times 2n$ complex transfer matrix, that is,

$$\mathbf{G}(s) = \mathrm{diag}\left\{ \begin{matrix} \cdots, G(s-j2\omega_1), G(s), G(s+j2\omega_1), \ldots, \\ \cdots, G(s-j4\omega_1), G(s-j2\omega_1), G(s), \ldots \end{matrix} \right\} \tag{20}$$

which is a diagonal matrix with different frequency shifts. The off-diagonal elements are zero since the LTI system does not contribute to any frequency couplings. The form of (20) applies to the transfer functions of the CC, the time delay, and the converter plants, which are represented by $G_{\mathrm{i}}(s)$, $G_{\mathrm{d}}(s)$, $Y_{\mathrm{o}}(s)$, and $Y_{\mathrm{p}}(s)$, respectively [18].

Combining the PLL and CC, the closed-loop model of the VSC can be derived as shown in Fig. 11, from which the VSC admittance can be deduced as

$$\begin{aligned} \mathbf{Y}(s) &= -\frac{\begin{bmatrix} \hat{\mathbf{i}} \\ e^{j2\theta^+}\hat{\mathbf{i}}^* \end{bmatrix}}{\begin{bmatrix} \hat{\mathbf{v}}^g \\ e^{j2\theta^+}\hat{\mathbf{v}}^{g*} \end{bmatrix}} \\ &= (\mathbf{I} + \mathbf{Y}_{\mathrm{p}}\mathbf{G}_{\mathrm{d}}\mathbf{G}_{\mathrm{i}})^{-1}(\mathbf{Y}_{\mathrm{o}} - \mathbf{Y}_{\mathrm{p}}\mathbf{G}_{\mathrm{d}}\mathbf{G}_{\mathrm{i}}\mathbf{Y}_{\mathrm{PLL}}). \end{aligned} \tag{21}$$

TABLE III
VSC PARAMETERS

Parameters	Symbols	Values
Inverter L filter	L	3 mH
DC voltage	V_{dc}	680 V
Current reference	$I_{d\mathrm{ref}}$ / $I_{q\mathrm{ref}}$	10 A / 0 A
Current PR Controller	K_{pi} / K_{ri}	5 Ω / 800 Ω/s
Switching/sampling frequency	f_s	10 kHz

C. Generalization of Proposed Modeling Method

It is important to note that the form of (19) applies to all ac variables shown in Fig. 11, i.e., the VSC is represented by a 2×2 model in the time domain with complex vectors, or a $2n \times 2n$ model in the frequency domain. Although only the PLL dynamic is considered in this work, the proposed approach also applies to other kinds of outer-loop controls [18].

On the other hand, the VSC model can be seen as a generalization of the unified $\alpha\beta$-frame model proposed by Wang *et al.* [5] to unbalanced grids. The model in [5] applies only to three-phase balanced grids, where the input variable can be regarded as a special case of (19) with $k = 0$, and each complex vector merely corresponds to one frequency component.

V. MODEL VALIDATION

An L-filtered VSC with a three-phase unbalanced grid voltage is studied in this section for the model validation. The control is implemented as shown in Fig. 1, where the SRF-PLL and the Notch-SRF-PLL are compared under Cases A–C. Parameters of the VSC are listed in Table III.

A. Frequency Scan Validation

The frequency scan is performed in simulation first to validate the VSC admittance model. Case A is considered for both SRF-PLL and Notch-SRF-PLL.

1) Model Order Selection: Based on the spectrum of $V_d^c(t)$ in Fig. 4(b) for Case A, the SRF-PLL can be modeled with a truncated 5×5 HTF matrix. The HTFs of $\mathcal{V}_d^c$, $\mathcal{T}_{\Delta\theta}$, and $\mathcal{T}_{\Delta\theta}^*$ are obtained through the discrete-time Fourier transformation (DFT) analysis applied to the steady-state trajectories, which are all 5×5 matrices.

For the Notch-SRF-PLL in Case A, Fig. 5(b) indicates that $V_d^c(t)$ consists only of components at 0 rad/s and $\pm 2\omega_1$ in steady state. Thus, the HTF model order for the Notch-SRF-PLL is only three. $\mathcal{V}_d^c$ can be determined through the DFT analysis of $V_d^c(t)$. $\mathcal{T}_{\Delta\theta}$ and $\mathcal{T}_{\Delta\theta}^*$ are identity matrices.

2) Frequency Scan: The derived admittance model of (21) can be validated by the frequency-scan approach: a three-phase voltage-source perturbation is injected into the VSC system by $\mathbf{v}_p$. When $\mathbf{v}_p$ consists only of a positive-sequence voltage input at a frequency of ω, corresponding to $\mathbf{V}^g(s)$ only, the output current responses at different frequencies will be generated; thus, the $(k+1)$th column of $\mathbf{Y}(s)$ can be validated by the frequency scan. Similarly, other columns of the admittance matrix can be validated by injecting $\mathbf{v}_p$ at different frequencies.

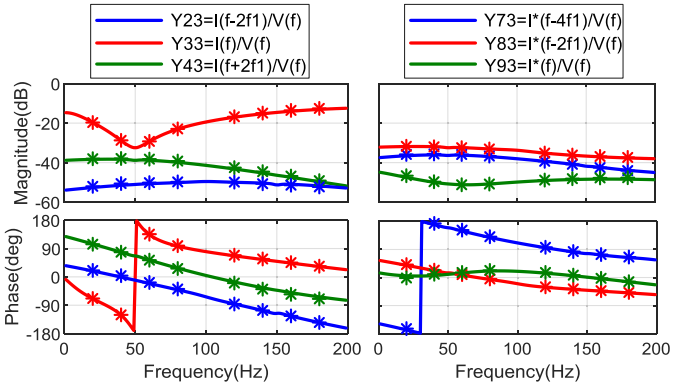

Fig. 12. Frequency-scanned results of $\mathbf{Y}(s)$ with SRF-PLL for Case A.

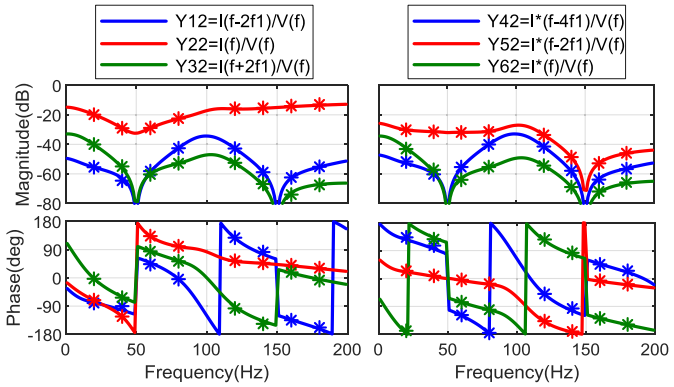

Fig. 13. Frequency-scanned results of $\mathbf{Y}(s)$ with Notch-SRF-PLL for Case A.

Since the frequency coupling is most significant around the fundamental frequency, $\mathbf{v}_p$ is swept from 20 to 180 Hz for validation. For the SRF-PLL, the HTF order is 5 for Case A; the VSC admittance model should be characterized by a 10×10 matrix. For brevity, only six dominant elements in the third column of $\mathbf{Y}(s)$ are validated, as shown in Fig. 12. The solid lines denote the analytical models, and the asterisks denote the frequency-scanned results. It is seen that the measured results agree well with the models.

For the Notch-SRF-PLL, the HTF order is only 3, the VSC admittance model can thus be represented by a 6×6 matrix. Each element of the second column of $\mathbf{Y}(s)$ is validated in Fig. 13. The measured results also align well with the analytical models. Therefore, the proposed model can accurately capture the frequency-coupling dynamics in the VSC.

B. Impacts of PLL Structure and VUF

Comparing the blue and green lines in Figs. 12 and 13, it is found that the Notch-SRF-PLL can mitigate the frequency couplings around the fundamental frequency, as the notch filter helps reduce the harmonics in the VSC steady-state trajectories.

The VUF (V^-/V^+) also affects significantly on the VSC steady-state trajectory, whose impacts are studied with Case B.

For the SRF-PLL, when the negative-sequence grid voltage decreases to 0.1 p.u. (Case B), the dominant harmonics of $V_d^c(t)$ only contain 0 rad/s and $\pm 2\omega_1$, as shown in Fig. 4(b).

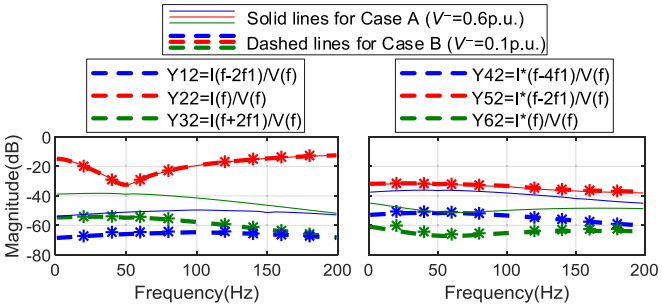

Fig. 14. Frequency-scanned results of $\mathbf{Y}(s)$ with SRF-PLL for Case B compared with Case A.

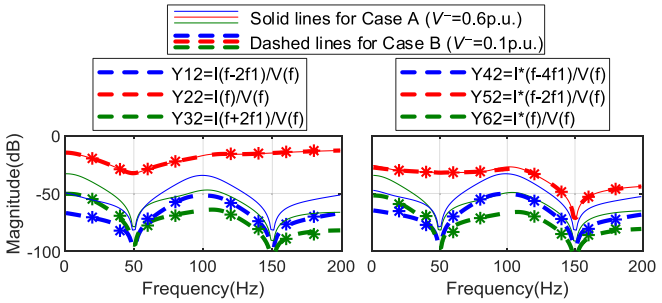

Fig. 15. Frequency-scanned results of $\mathbf{Y}(s)$ with Notch-SRF-PLL for Case B compared with Case A.

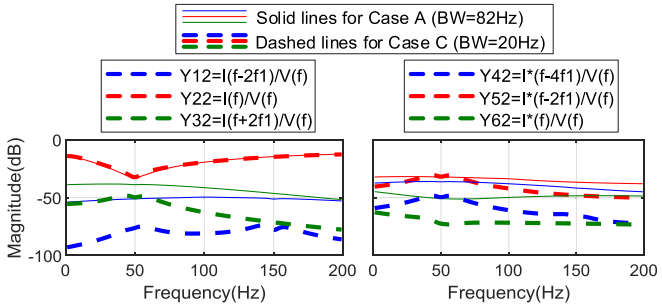

Fig. 16. $\mathbf{Y}(s)$ with SRF-PLL for Case C compared with Case A.

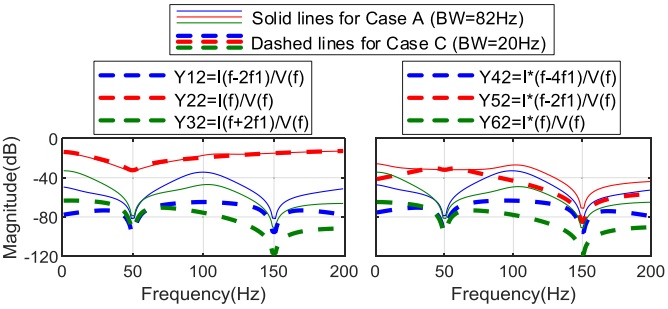

Fig. 17. $\mathbf{Y}(s)$ with Notch-SRF-PLL for Case C compared with Case A.

Thus, the HTF model can be truncated as a 3×3 matrix, and the VSC admittance model is characterized by a 6×6 matrix. The second column of $\mathbf{Y}(s)$ is displayed in Fig. 14 with the dashed lines. Here, only magnitude plots are shown for brevity. It is found that the measured results denoted by the asterisks agree well with the analytical models, and thus taking the order

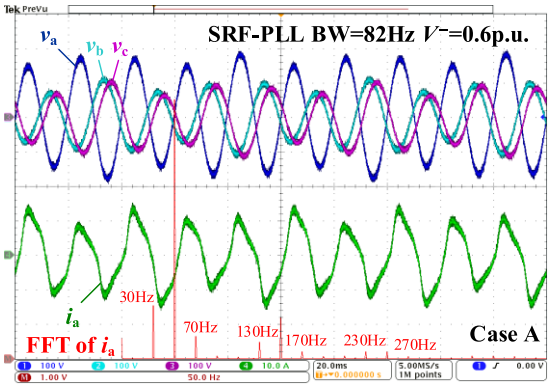

(a)

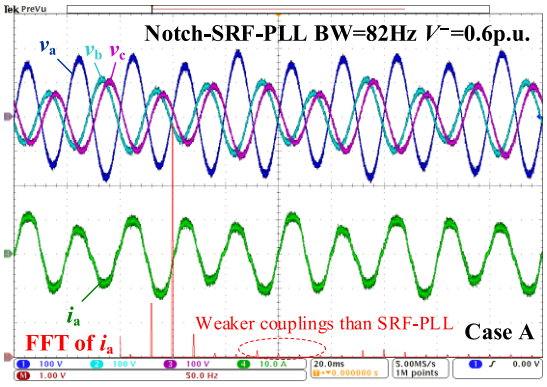

(b)

Fig. 18. Experimental waveforms for Case A. (a) SRF-PLL. (b) Notch-SRF-PLL.

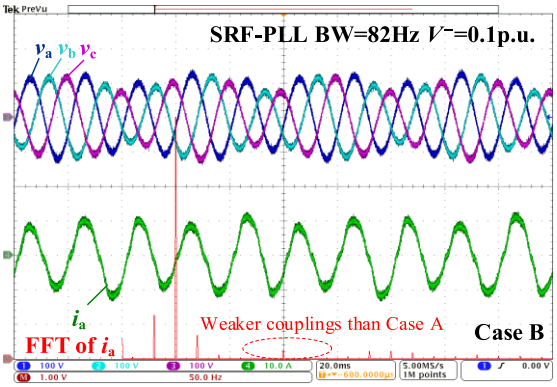

(a)

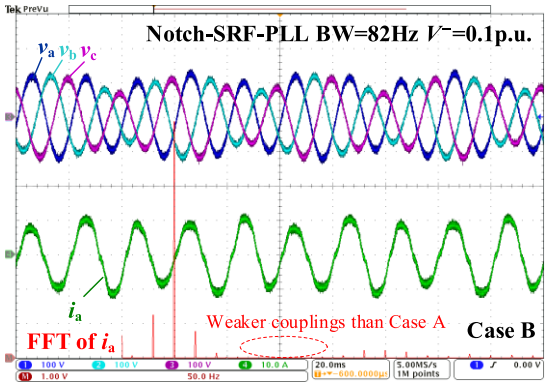

(b)

Fig. 19. Experimental waveforms for Case B. (a) SRF-PLL. (b) Notch-SRF-PLL.

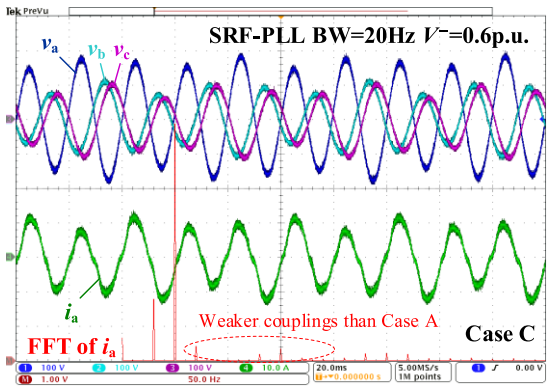

(a)

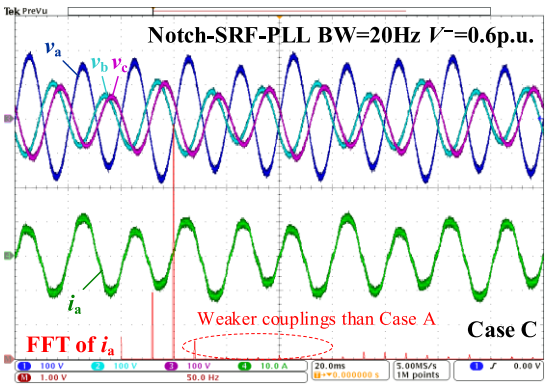

(b)

Fig. 20. Experimental waveforms for Case C. (a) SRF-PLL. (b) Notch-SRF-PLL.

of $n = 3$ is adequate for capturing the dynamic couplings of the VSC.

In addition, the VSC admittance model for Case A is also provided in Fig. 14 by solid lines for comparison. It is found that the VUF severely affects the magnitudes of the blue and green lines but has little impact on the red lines. This is because the couplings represented by the red lines are the dominant ones contributed by the steady-state positive-sequence voltage. The other couplings denoted by the blue and green lines are introduced by the steady-state negative- sequence voltage, which largely relies on the VUF. The larger the VUF is, the stronger the couplings will be.

For the Notch-SRF-PLL, similar effects impacted by the VUF can be found in Fig. 15. When V^- decreases to 0.1 p.u., the magnitudes of the blue and green lines decrease accordingly, indicating weaker couplings.

C. Impacts of PLL BW

In addition to the VUF, the control BW of the PLL also affects the dynamic couplings of the VSC, which are analyzed with Case C.

The steady-state analysis for the SRF-PLL in Fig. 4 shows that the decrease of the PLL BW mitigates the higher order harmonics in $V_d^c(t)$; thus, the PLL can also be truncated as a 3×3 HTF model. The magnitudes of the admittance elements for the SRF-PLL are shown in Fig. 16. The dashed lines denote the models for Case C, and the solid lines denote the models for Case A. It is found that except the interactions at the same frequency (i.e., Y_{22} in the left figure), all the couplings with other frequencies are largely mitigated by decreasing the PLL BW.

For the Notch-SRF-PLL, the admittance analyses for Case C compared with Case A is provided in Fig. 17, where the couplings among different frequencies are also weakened as the PLL BW decreases.

D. Experimental Validation

Experimental tests are provided for validating the frequency coupling phenomena. The same scenarios as Cases A–C are performed in experiments. The unbalanced grid voltages are generated by the grid simulator Chroma 61845, which enables to inject an interharmonic perturbation at 30 Hz simultaneously. The perturbed three-phase grid voltage and phase-A current waveforms for different cases are shown in Figs. 18–20.

In Fig. 18(a), there is an obvious component of 150 Hz in the spectrum of i_a, which is caused by the poor attenuation of the negative-sequence fundamental-frequency voltage in SRF-PLL. Such a negative-sequence voltage can propagate through the PLL and thus generate the positive-sequence triplen harmonic in the current response. It is also found that the voltage perturbation at 30 Hz excites responses at different frequencies in the current, i.e., 30, 70, 130, and 170 Hz. These detected frequency components are well predicted by the proposed model. In contrast, the Notch-SRF-PLL effectively attenuates the negative-sequence fundamental-frequency voltage. Hence, the frequency component at 150 Hz is almost zero in Fig. 18(b), and the frequency couplings in the dashed ellipse become weaker.

For Case B, the spectrum of i_a shown in Fig. 19 indicates that the decrease of VUF results in weaker frequency couplings except at $|f-2f_1|$ for both SRF-PLL and Notch-SRF-PLL. For Case C, the spectrum of i_a shown in Fig. 20 indicates that a lower BW of the PLL can weaken all the frequency couplings in the VSC. These results further validate the above theoretical analyses.

VI. Stability Analysis

The stability on a grid-connected VSC operating under an unbalanced grid condition is analyzed with the proposed model. The system configuration is shown in Fig. 21, where the unbalanced grid impedance (L_{ga}, L_{gb}, L_{gc}) is considered. Circuit parameters are listed in Table IV.

To perform the impedance-based stability analysis, the point of common coupling (PCC) is selected between L and C_f.

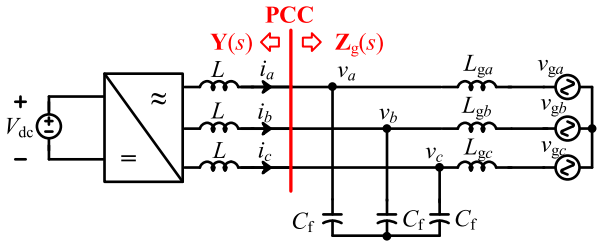

Fig. 21. Unbalanced grid-connected VSC system for stability analysis.

TABLE IV
VSC Parameters for Stability Analysis

Parameters	Symbols	Values
Grid voltage (line-to-line)	V_g	100 V
Steady-state PCC voltage	V^+ / V^- (VUF)	70 V / 19.15 V (27.4%)
Grid impedance	L_{ga} / L_{gb} / L_{gc}	12 mH / 12 mH / 24 mH
Inverter L filter	L	2 mH
Inverter C filter	C_f	10 μF
DC voltage	V_{dc}	680 V
Current reference	I_{dref} / I_{qref}	15 A / 0 A
Current PR Controller	K_{pi} / K_{ri}	5 Ω / 800 Ω/s
PLL bandwidth	BW	10 Hz / 8 Hz
Switching/sampling frequency	f_s	10 kHz

The steady-state PCC voltage is analyzed first by simulation, which is used for modeling $\mathbf{Y}(s)$, and the VUF is found to be around 27.4% as given in the table.

A. Grid Impedance Model

As the grid impedance is unbalanced, how to derive $\mathbf{Z}_g(s)$ is briefly introduced.

The symmetrical component decomposition [26] is first applied. Supposing unbalanced three-phase impedances as $Z_a(s)$, $Z_b(s)$, and $Z_c(s)$ for each phase, and by defining $a = e^{j2\pi/3}$, it can be derived that

$$\begin{bmatrix} \mathbf{V}(s) \\ \mathbf{V}^*(s) \end{bmatrix} = \frac{1}{3} \begin{bmatrix} Z_{11}(s) & Z_{12}(s) \\ Z_{21}(s) & Z_{22}(s) \end{bmatrix} \begin{bmatrix} \mathbf{I}(s) \\ \mathbf{I}^*(s) \end{bmatrix} \tag{22}$$

where $Z_{11}(s) = Z_{22}(s) = Z_a(s) + Z_b(s) + Z_c(s)$, $Z_{12}(s) = Z_a(s) + a^2 Z_b(s) + aZ_c(s)$, and $Z_{21}(s) = Z_a(s) + aZ_b(s) + a^2 Z_c(s)$. Then (22) can be extended with the same input vector as (19), yielding (23) shown at the bottom of the next page.

Consequently, the grid impedance can be derived as

$$\mathbf{Z}_g(s) = (\mathbf{Z}_{Lg}^{-1}(s) + \mathbf{Y}_{Cf}(s))^{-1} \tag{24}$$

in which both $\mathbf{Z}_{Lg}(s)$ and $\mathbf{Y}_{Cf}(s)$ are derived according to (23).

B. Stability Analysis

As $\mathbf{Z}_g(s)\mathbf{Y}(s)$ is the minor loop gain of the system, the stability can be checked by the generalized Nyquist stability criterion (GNSC) applied to $\mathbf{Z}_g(s)\mathbf{Y}(s)$, or the analysis of right-half-plane (RHP) zeros of $\det(\mathbf{I} + \mathbf{Z}_g(s)\mathbf{Y}(s))$ [27].

Considering a practical unbalanced system, the Notch-SRF-PLL is used; thus, the impedances are derived with the order of 6. Fig. 22 shows the stability analysis by the GNSC, with the PLL BWs of 10 and 8 Hz. It is seen

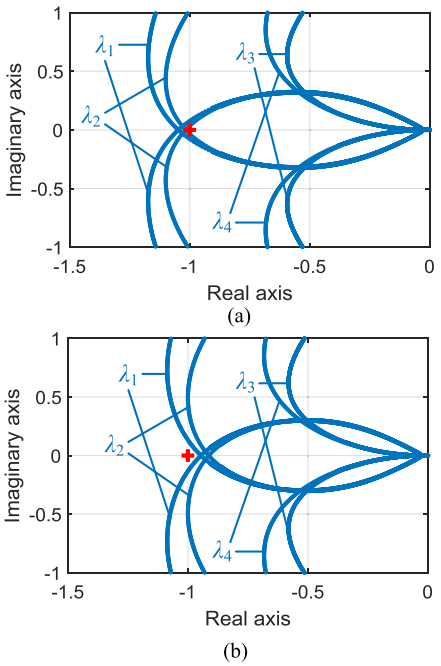

Fig. 22. Stability analysis with minor loop gain. (a) BW = 10 Hz. (b) BW = 8 Hz.

that when BW = 10 Hz, the Nyquist trajectories of the eigenvalues λ_1 and λ_2 encircle the critical point $(-1, 0)$, indicating instability. When BW decreases to 8 Hz, these two Nyquist trajectories do not encircle the critical point; thus, the system can be stabilized.

The analyses of $\det(\mathbf{I} + \mathbf{Z}_g(s)\mathbf{Y}(s))$ are also presented for identifying the oscillation frequency in Fig. 23. For BW = 10 Hz, the RHP zeros can be found at 44, 56, 143.6, and 156 Hz. For BW = 8 Hz, only left-half-plane (LHP) zeros are found, indicating a stable system.

Simulations are carried out with BW = 10 Hz and BW = 8 Hz, in Figs. 24 and 25, respectively. It is seen that for BW = 10 Hz, oscillations can be found in the VSC output voltages and currents. By analyzing the spectrum of i_a, the oscillation frequencies of 44.3, 55.9, 144.3, and 156 Hz are all identified, as shown in Fig. 24(b), which closely agree with the analyzed results in Fig. 23(a). The magnitudes at 144.3 and 156 Hz are very low since these coupling components are well attenuated by the Notch-SRF-PLL, as illustrated by Figs. 18(b)–20(b).

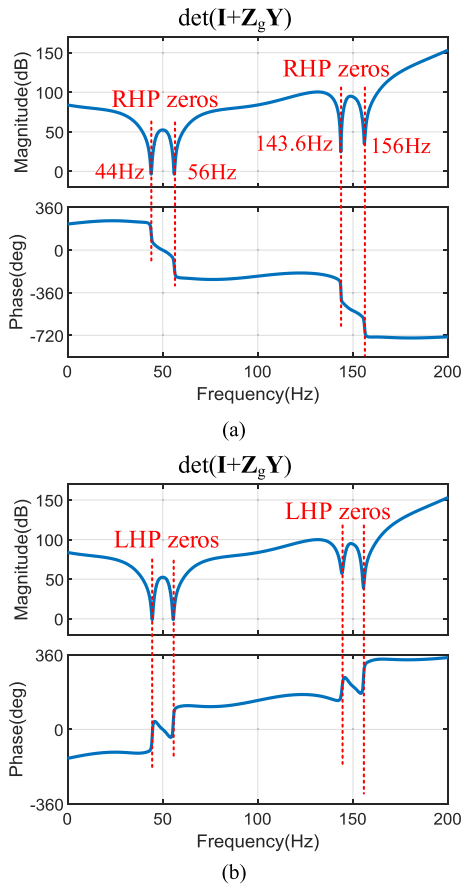

Fig. 23. Stability analysis with $\det(\mathbf{I} + \mathbf{Z}_g\mathbf{Y})$. (a) BW = 10 Hz. (b) BW = 8 Hz.

The stability analysis indicates the same conclusion for VSC controller design in balanced grids, that is, the lower PLL BW can achieve better stability in terms of the VSC-grid interaction [1]. Without loss of generality, other VSC control parameters can be analyzed with the same stability analysis approach.

The case study also shows how to use the proposed model for dynamic studies of unbalanced converter-based systems. A prominent feature of the model can be seen from this case, that is, the VSC admittance is merely dependent on its own input voltage trajectory. Consequently, it can be readily used for stability analysis when the VSC is connected to any other systems under various unbalanced grid structures.

$$\mathbf{Z}(s) = \frac{1}{3}\begin{bmatrix} \cdots & & & \cdots & & \\ & Z_{11}(s - j2\omega_1) & & & Z_{12}(s - j2\omega_1) & \\ & & Z_{11}(s) & & & Z_{12}(s) \\ & & & Z_{11}(s + j2\omega_1) & & \cdots \\ & & & \cdots & & \\ & & & \cdots & & \\ \cdots & & & Z_{22}(s - j4\omega_1) & & \\ & Z_{21}(s - j2\omega_1) & & & Z_{22}(s - j2\omega_1) & \\ & & Z_{21}(s) & & & Z_{22}(s) \\ & & & \cdots & & \cdots \end{bmatrix} \tag{23}$$

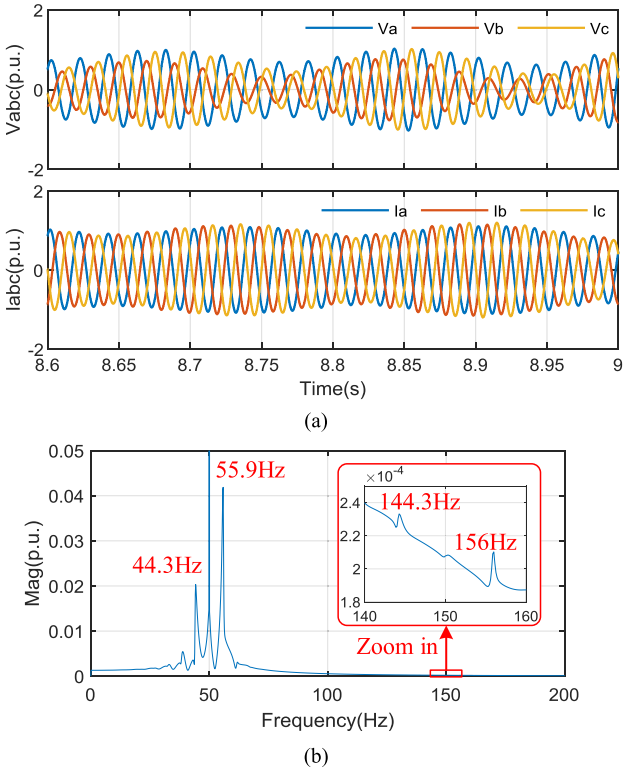

Fig. 24. Unstable simulation results with BW = 10 Hz. (a) Time-domain waveforms. (b) Spectrum of i_a.

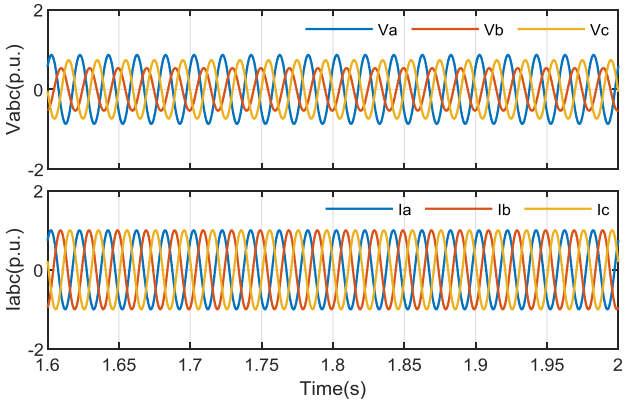

Fig. 25. Stable simulation results with BW = 8 Hz.

VII. Conclusion

This article presented a multifrequency complex-valued admittance model for a VSC with unbalanced grid voltages. The model is represented in the frequency domain with a $2n \times 2n$ matrix, which captures the frequency coupling effects caused by both the unbalanced operating trajectory and the asymmetric controls in the *dq* frame. It has been demonstrated in the frequency scan and experiments that the VUF and the PLL structure significantly affects the frequency-coupling dynamics in the VSC, which determines the model order of the HTF matrix. Furthermore, an important advantage is that the model is merely dependent on the steady-state operating trajectory of the VSC, which is verified by a case study on the stability analysis of an unbalanced grid-connected inverter system.

References

[1] X. Wang and F. Blaabjerg, "Harmonic stability in power electronic-based power systems: Concept, modeling, and analysis," *IEEE Trans. Smart Grid*, vol. 10, no. 3, pp. 2858–2870, May 2019.

[2] S. Hiti, D. Boroyevich, and C. Cuadros, "Small-signal modeling and control of three-phase PWM converters," in *Proc. IEEE Ind. Appl. Soc. Annu. Meeting*, Denver, CO, USA, Oct. 1994, pp. 1143–1150.

[3] L. Harnefors, M. Bongiorno, and S. Lundberg, "Input-admittance calculation and shaping for controlled voltage-source converters," *IEEE Trans. Ind. Electron.*, vol. 54, no. 6, pp. 3323–3334, Dec. 2007.

[4] B. Wen, D. Boroyevich, R. Burgos, P. Mattavelli, and Z. Shen, "Analysis of D–Q small-signal impedance of grid-tied inverters," *IEEE Trans. Power Electron.*, vol. 31, no. 1, pp. 675–687, Jan. 2016.

[5] X. Wang, L. Harnefors, and F. Blaabjerg, "Unified impedance model of grid-connected voltage-source converters," *IEEE Trans. Power Electron.*, vol. 33, no. 2, pp. 1775–1787, Feb. 2018.

[6] S. Sudhoff, "Multiple reference frame analysis of an unsymmetrical induction machine," *IEEE Trans. Energy Convers.*, vol. 8, no. 3, pp. 425–432, Sep. 1993.

[7] E. V. Larsen, D. H. Baker, and J. C. Mciver, "Low-order harmonic interactions on AC/DC systems," *IEEE Trans. Power Del.*, vol. 4, no. 1, pp. 493–501, Jan. 1989.

[8] L. Harnefors, "Modeling of three-phase dynamic systems using complex transfer functions and transfer matrices," *IEEE Trans. Ind. Electron.*, vol. 54, no. 4, pp. 2239–2248, Aug. 2007.

[9] A. M. Stankovic and T. Aydin, "Analysis of unbalanced power system faults using dynamic phasors," *IEEE Trans. Power Syst.*, vol. 15, no. 3, pp. 1062–1068, Aug. 2000.

[10] A. M. Stankovic, S. R. Sanders, and G. C. Verghese, "Dynamic phasors in modeling and analysis of unbalanced polyphaser AC machines," *IEEE Trans. Energy Convers.*, vol. 17, no. 1, pp. 107–113, Mar. 2002.

[11] P. Stefanov and A. Stankovic, "Modeling of UPFC operation under unbalanced conditions with dynamic phasors," *IEEE Trans. Power Syst.*, vol. 17, no. 2, pp. 395–403, May 2002.

[12] S. Sanders, J. Noworolski, X. Liu, and G. Verghese, "Generalized averaging method for power conversion circuits," *IEEE Trans. Power Electron.*, vol. 6, no. 2, pp. 251–259, Apr. 1991.

[13] N. M. Wereley, "Analysis and control of linear periodically time varying systems," Ph.D. dissertation, Dept. Aeronaut. Astronaut., MIT, Cambridge, MA, USA, 1991.

[14] E. Mollerstedt and B. Bernhardsson, "Out of control because of harmonics-an analysis of the harmonic response of an inverter locomotive," *IEEE Control Syst. Mag.*, vol. 20, no. 4, pp. 70–81, Aug. 2000.

[15] J. Kwon, X. Wang, F. Blaabjerg, C. L. Bak, V.-S. Sularea, and C. Busca, "Harmonic interaction analysis in a grid–connected converter using harmonic state-space (HSS) modeling," *IEEE Trans. Power Electron.*, vol. 32, no. 9, pp. 6823–6835, Sep. 2017.

[16] J. Kwon, X. Wang, F. Blaabjerg, C. L. Bak, A. R. Wood, and N. R. Watson, "Linearized modeling methods of AC–DC converters for an accurate frequency response," *IEEE J. Emerg. Sel. Topics Power Electron.*, vol. 5, no. 4, pp. 1526–1541, Dec. 2017.

[17] D. Lu, X. Wang, and F. Blaabjerg, "Impedance-based analysis of DC–link voltage dynamics in voltage-source converters," *IEEE Trans. Power Electron.*, vol. 34, no. 4, pp. 3973–3985, Apr. 2019.

[18] Y. Liao and X. Wang, "Stationary-frame complex-valued frequency-domain modeling of three-phase power converters," *IEEE J. Emerg. Sel. Topics Power Electron.*, early access, 2019, doi: 10.1109/jestpe.2019.2958938.

[19] H. Wu and X. Wang, "Dynamic impact of zero-sequence circulating current on modular multilevel converters: Complex-valued AC impedance modeling and analysis," *IEEE J. Emerg. Sel. Topics Power Electron.*, early access, 2019, doi: 10.1109/JESTPE.2019.2951446.

[20] O. Troeng, B. Bernhardsson, and C. Rivetta, "Complex-coefficient systems in control," in *Proc. Amer. Control Conf. (ACC)*, Seattle, WA, USA, May 2017, pp. 1721–1727.

[21] A. Rygg, "Impedance-based methods for small-signal analysis of systems dominated by power electronics," Ph.D. dissertation, Dept. Eng. Cybern., Norwegian Univ. Sci. Technol., Trondheim, Norway, 2018.

[22] C. Zhang, M. Molinas, A. Rygg, J. Lyu, and X. Cai, "Harmonic transfer function-based impedance modelling of a three-phase VSC for asymmetric AC grids stability analysis," *IEEE Trans. Power Electron.*, vol. 34, no. 12, pp. 12552–12566, Dec. 2019, doi: 10.1109/TPEL.2019.2909576.

[23] Y. Liao, X. Wang, X. Yue, and H. Gong, "Harmonic transfer-function model of three-phase synchronous reference frame PLL under unbalanced grid conditions," in *Proc. IEEE Appl. Power Electron. Conf. Expo. (APEC)*, Anaheim, CA, USA, Mar. 2019, pp. 58–65.

[24] M. H. Hirsch, S. Smale, and R. L. Devaney, *Differential Equations, Dynamical Systems & an Introduction to Chaos*, 3rd ed. Amsterdam, The Netherlands: Elsevier, 2013.
[25] X. Yue, X. Wang, and F. Blaabjerg, "Review of small–signal modeling methods including frequency–coupling dynamics of power converters," *IEEE Trans. Power Electron.*, vol. 34, no. 4, pp. 3313–3328, Apr. 2019.
[26] G. Paap, "Symmetrical components in the time domain and their application to power network calculations," *IEEE Trans. Power Syst.*, vol. 15, no. 2, pp. 522–528, May 2000.
[27] Y. Liao and X. Wang, "Impedance-based stability analysis for interconnected converter systems with open-loop RHP poles," *IEEE Trans. Power Electron.*, early access, 2019, doi: 10.1109/TPEL.2019.2939636.

Yicheng Liao (Student Member, IEEE) received the B.S. degree in electrical engineering and its automation, and the M.S. degree in electrical engineering from Southwest Jiaotong University, Chengdu, China, in 2015 and 2018, respectively. She is currently pursuing the Ph.D. degree in power electronic engineering with Aalborg University, Aalborg, Denmark.

She was a Visiting Student with the École Polytechnique and Inria, Paris, France, in July 2017. She has been a Research Assistant with the Department of Energy Technology, Aalborg University, since September 2018. Her research interests include the modeling, stability analysis, and control of power electronics-based power systems.

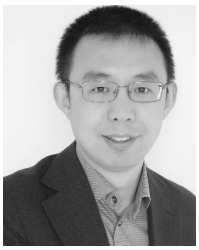

Xiongfei Wang (Senior Member, IEEE) received the B.S. degree in electrical engineering from Yanshan University, Qinhuangdao, China, in 2006, the M.S. degree in electrical engineering from the Harbin Institute of Technology, Harbin, China, in 2008, and the Ph.D. degree in energy technology from Aalborg University, Aalborg, Denmark, in 2013.

Since 2009, he has been with the Department of Energy Technology, Aalborg University, where he became an Assistant Professor in 2014, an Associate Professor in 2016, and a Professor and the Research Program Leader of the Electronic Power Grid (eGrid) in 2018, and the Director of Aalborg University-Huawei Energy Innovation Center in 2020. His current research interests include modeling and control of grid-interactive power converters, stability and power quality of converter-based power systems, and active and passive filters.

Dr. Wang was selected into the Aalborg University Strategic Talent Management Program in 2016. He has received the six IEEE prize paper awards, the 2016 Outstanding Reviewer Award of the IEEE TRANSACTIONS ON POWER ELECTRONICS, the 2018 IEEE PELS Richard M. Bass Outstanding Young Power Electronics Engineer Award, the 2019 IEEE PELS Sustainable Energy Systems Technical Achievement Award, and the 2019 Highly Cited Researcher by Clarivate Analytics (former Thomson Reuters). He serves as a Member-at-Large for Administrative Committee of the IEEE Power Electronics Society from 2020 to 2022, and an Associate Editor for the IEEE TRANSACTIONS ON POWER ELECTRONICS, the IEEE TRANSACTIONS ON INDUSTRY APPLICATIONS, and the IEEE JOURNAL OF EMERGING AND SELECTED TOPICS IN POWER ELECTRONICS.

Xiaolong Yue received the bachelor's and Ph.D. degrees in electrical engineering from Xi'an Jiaotong University (XJTU), Xi'an, China, in 2011 and 2017, respectively.

From 2011 to 2017, he was a Research Assistant with XJTU. From 2015 to 2016, he was a Visiting Ph.D. Student with the Center for Power Electronics Systems (CPES), Virginia Tech, Blacksburg, VA, USA. From 2017 to 2018, he was a Post-Doctoral Fellow with the Department of Energy Technology, Aalborg University, Aalborg, Denmark. Since 2018, he has been a Power Design Engineer with Ericsson AB, Gothenburg, Sweden. His research interests include the stability of ac and dc power systems, modeling and control of power electronics converters and systems, and impedance measurement for power electronic-based systems.

Lennart Harnefors (Fellow, IEEE) received the M.Sc., Licentiate, and Ph.D. degrees in electrical engineering from the Royal Institute of Technology (KTH), Stockholm, Sweden, and the Docent (D.Sc.) degree in industrial automation from Lund University, Lund, Sweden, in 1993, 1995, 1997, and 2000, respectively.

From 1994 to 2005, he was with Mälardalen University, Västerås, Sweden, where he has been a Professor of electrical engineering since 2001. From 2001 to 2005, he was, in addition, a part-time Visiting Professor of electrical drives with the Chalmers University of Technology, Gothenburg, Sweden. Since 2005, he has been with ABB, Västerås, where he is currently a Senior Principal Scientist with Corporate Research. He is also a part-time Adjunct Professor of power electronics with KTH. His research interests include control and dynamic analysis of power electronic systems, particularly grid-connected converters and ac drives.

Dr. Harnefors is an Associate Editor of the *IET Electric Power Applications*.